

Discovering topological surface states of Dirac points

Hengbin Cheng,^{1,2} Yixin Sha,³ Rongjuan Liu,¹ Chen Fang,^{1,4} and Ling Lu^{1,4,*}

¹*Institute of Physics, Chinese Academy of Sciences/Beijing National Laboratory for Condensed Matter Physics, Beijing 100190, China*

²*School of Physical Sciences, University of Chinese Academy of Sciences, Beijing 100049, China*

³*School of Electronics Engineering and Computer Science, Peking University, Beijing 100871, China*

⁴*Songshan Lake Materials Laboratory, Dongguan, Guangdong 523808, China.*

(Dated: January 20, 2020)

Dirac materials, unlike the Weyl materials, have not been found in experiments to support intrinsic topological surface states, as the surface arcs in existing systems are unstable against symmetry-preserving perturbations. Utilizing the proposed glide and time-reversal symmetries, we theoretically design and experimentally verify an acoustic crystal of two frequency-isolated three-dimensional Dirac points with Z_2 monopole charges and four gapless helicoid surface states.

A three-dimensional (3D) Dirac point [1] disperses the same way as the solutions to the massless Dirac equation at the vicinity of the four-fold linear point degeneracy. Playing a central role in 3D band topology, Dirac points can, upon symmetry breaking, transition into Weyl points, line nodes or topological bandgaps with gapless surface states. Although 3D Dirac points have been experimentally discovered in electron [2–7], magnon [8, 9] and photonic [10] systems along with a variety of other theoretical proposals [11–23], none of the surface states are topological. Specifically, there have been no robust gapless surface bands associated with the bulk Dirac points [24–26].

The current lack of topological surface states for Dirac points can be understood through the anticrossing of two Weyl surface states. Illustrated in Fig. 1, the topological surface dispersion of a Weyl crystal is a doubly-periodic helicoid sheet whose singularities locates at the projection of the bulk Weyl points. The chirality of the helicoid around each Weyl point equals the sign of its Chern number. Since a Dirac point is composed of two Weyl points of opposite Chern numbers, the Dirac surface state should be composed of two helicoids of opposite chiralities. Two opposite helicoid surfaces generally cross each other along a line of momenta and anticross (hybridize with each other), resulting in gapped surface bands which are topologically trivial. The only exception was theoretically proposed in Ref. [27], in which the glide symmetries combined with the time-reversal (\mathcal{T}) can stabilize a degenerate line and protect the crossing of the helicoids. As illustrated in Fig. 1, one glide can protect double helicoids and two glides can protect quad-helicoid surfaces states.

In this work, we present an acoustic band structure with two ideal Z_2 Dirac points protected by glide reflections. The acoustic crystal is 3D-printed and the measured surface dispersions exhibit quad-helicoid surface sheets.

Ideal acoustic Dirac points The cubic cell of the acoustic crystal, in Fig. 2(a), consists of thick rods and thin sticks, belonging to space group $Ia\bar{3}$ (No. 206) of the

body-centered-cubic (BCC) lattice. The four thick rods of radius $0.15a$ point at the directions of the BCC lattice vectors, where a is the lattice constant of the cubic cell. These disconnected rods form the BPI (blue phase I of liquid crystal) photonic crystal in Ref. [28, 29]. We add the thin sticks to connect all rods and mechanically support the whole structure. The sticks are too thin, $0.025a$ in radius, to change the Dirac acoustic bands, as compared in Supplementary Materials. The background material is air and the interfaces are treated as sound hard-wall boundaries in numerical simulations.

There are two Dirac points locate at the $\pm P$ points of the BCC Brillouin zone [BZ, Fig. 2(b)], where four bands (from the fifth to the eighth in ascending energy order) meet, as shown in Fig. 2(c). The density of states (DOS) [30] vanishes at the Dirac frequency and grows quadratically away from it, as expected for linear dispersion relations.

The local Hamiltonian of this Dirac point is $H(\mathbf{k}) \sim \begin{pmatrix} \mathbf{k} \cdot \boldsymbol{\sigma} & 0 \\ 0 & -\mathbf{k} \cdot \boldsymbol{\sigma} \end{pmatrix}$, determined by the $k \cdot p$ analysis detailed in the Supplementary Materials. This four-fold degeneracy is joined, due to the anti-unitary parity-time symmetry (\mathcal{PT}), by two conjugated 2D representations of the little group. The little group of No. 206 at P also has a four fold representation which is the generalized Dirac point discussed in Ref. [28, 29]. The Dirac point has identical group velocities while the generalized one does not.

Each Dirac point is stabilized by the products of \mathcal{T} and the three non-commuting glides ($G_x = \{M_x|(a/2)\hat{x} + (a/2)\hat{y}\}$, $G_y = \{M_y|(a/2)\hat{x}\}$, $G_z = \{M_z|(a/2)\hat{y}\}$), denoted as $G_i\mathcal{T}$ ($i = x, y, z$). M_i are the mirror operations and the inversion $\mathcal{P} = G_x G_y G_z$. Each $G_i\mathcal{T}$ symmetry enforces a line degeneracy at the zone boundary, represented by the dashed lines in all figures consistently. The three degeneracy lines intersect at the P point, shown in Fig. 2(b), (e). We note that the P point have neither \mathcal{T} nor G_i symmetries by themselves.

Z_2 monopoles Dirac point is the symmetry-protected Z_2 monopole in the 3D momentum space [31–33]. However, the Z_2 symmetries in the these systems (\mathcal{PT} for

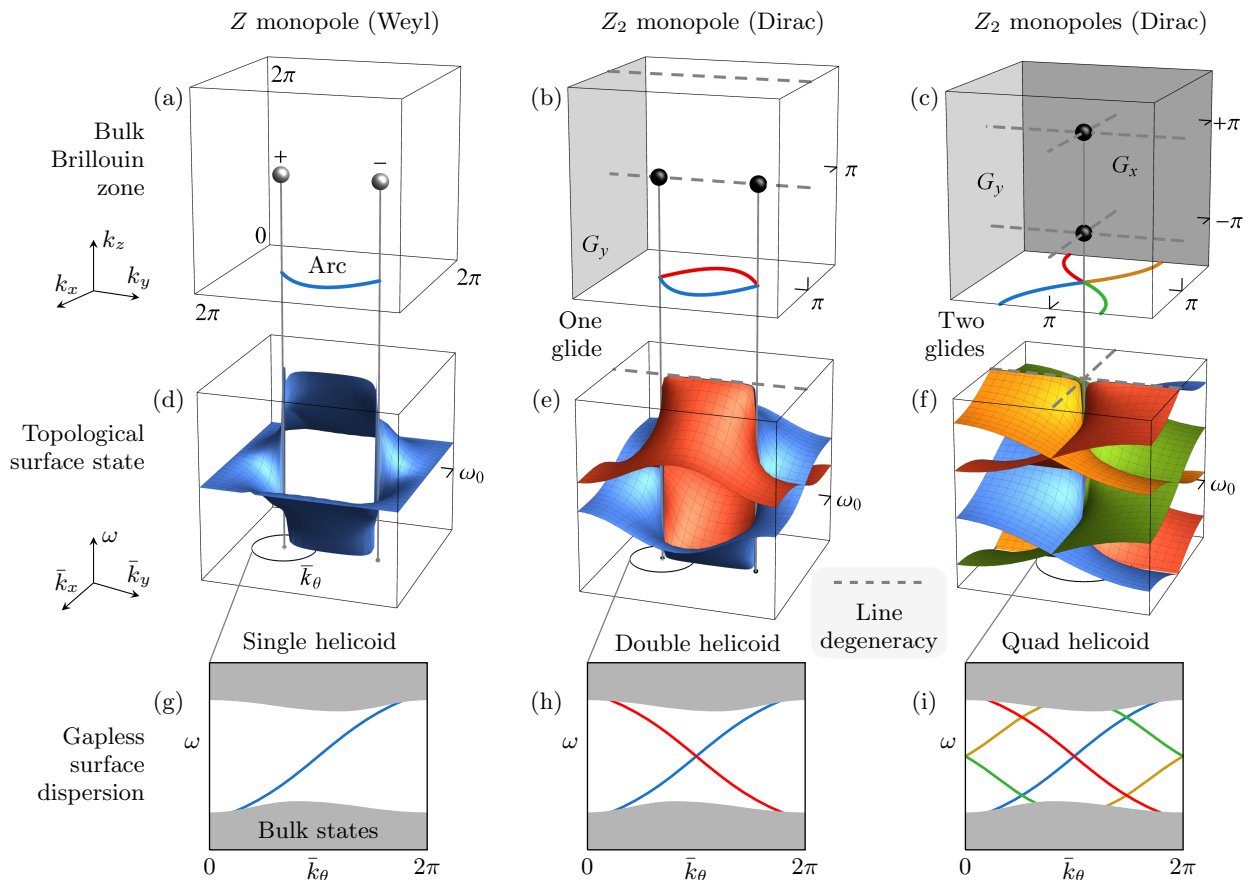


FIG. 1. Bulk monopoles and helicoid surfaces. (a), (b), (c) are the 3D BZ containing two Z or Z_2 monopoles. (a), (b) can be the BZs of cubic lattices, while (c) is the BZ of the BCC lattice in our acoustic design. The arcs, at the bottom plane, are the iso-frequency contours of the helicoid surface states at frequency ω_0 labeled in (d), (e), (f). The glide planes are fill in gray and the $G_i\mathcal{T}$ protected line degeneracies are shown in dashed gray lines. (g), (h), (i) illustrates the gapless surface dispersions, around the projected monopoles, along a circular path of \bar{k}_θ in the surface BZ. The Z monopoles can be Weyl points, nodal lines or surfaces. The Z_2 monopoles can be Dirac points, Z_2 nodal lines or Weyl dipoles.

example) cannot protect any line degeneracies on the surface, disallowing the gapless connectivity between two helicoids of opposite chiralities. In contrast, the Z_2 invariant of our acoustic Dirac point is protected by $G_i\mathcal{T}$ [27], leading to the nontrivial band topology not only in the bulk but also on the surface.

In Fig. 2(d), we calculate the non-Abelian Berry phase [34] of the lower two bands (5th and 6th) on a sphere enclosing the Dirac point. The gapless spectra indicate the nontrivial monopole charge of $Z_2 = 1$. Since this Z_2 charge can be protected by either one of the three $G_i\mathcal{T}$ [27], we can break the other two or one $G_i\mathcal{T}$ to get the Z_2 nodal ring [35–39] and Weyl dipoles [27, 31]. These symmetry-breaking cases are illustrated in Fig. 2 (e), (f), (g) and discussed in detail in the Supplementary Materials.

Quad-helicoid and Jacobi elliptic function We project the two Dirac points onto the (001) surface, corresponding to the case in Fig. 1 (c), (f), (i). The plane group of

this surface is $p2gg$, on which the two degenerate lines due to $G_x\mathcal{T}$ and $G_y\mathcal{T}$ are presented. These two line degeneracies, outlining the whole boundaries of the surface BZ, protect all the crossings among the four helicoid surface sheets. The iso-frequency contour, in Fig. 1(c), are four branches originating from the projected Dirac points. The four branches are connected across the zone boundary forming two non-contractable loops.

If we parametrize the 2D surface BZ as a complex plane ($z \propto k_x + ik_y$) [27], the helicoid surface bands can be expressed as (are topologically equivalent to) the double-periodic elliptic functions [40, 41]. The four helicoids in Fig. 1(f) are plotted using the Jacobi elliptic functions $cn(z, \frac{1}{2})$. The Jacobi function has two zeros and two poles in one period, each locating at the center of each quadrant. These four singularities represent two Weyl dipoles and all project to the same point in the surface BZ. So we construct the quad-helicoid surfaces by stacking the four quadrants of the Jacobi func-

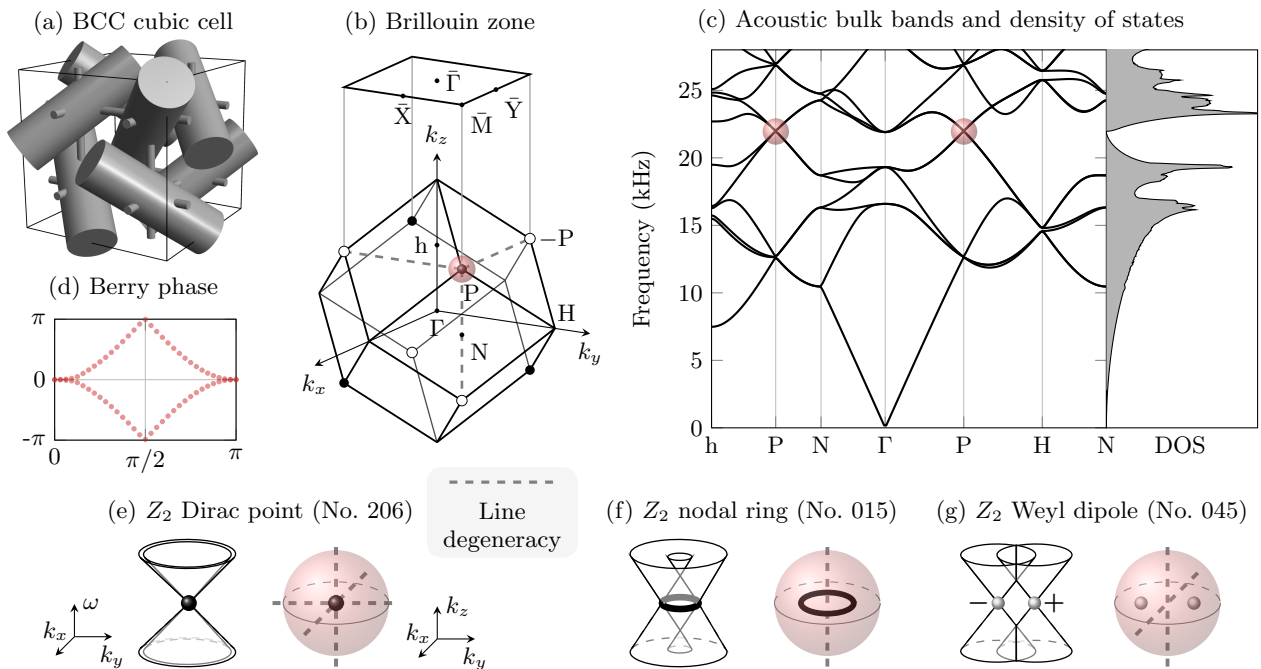


FIG. 2. Ideal acoustic Dirac points with Z_2 charges. (a) One cubic cell of the acoustic crystal of BCC lattice. (b) BCC BZ and the [001] surface BZ. The two $\pm P$ points project to the same point \bar{M} in the surface BZ. (c) Acoustic bulk band structure with the Dirac points crossing between the 5-6th and 7-8th bands at the P point. The DOS vanished at the frequency of ideal Dirac points. (d) Calculated non-Abelian Berry phases on the surface of the red sphere enclosing the Dirac point. Over the polar angle, the nontrivial winding of Berry phases implies topological invariant of $Z_2 = 1$. (e, f, g) Three types of four-bands nodal structures that carry Z_2 monopole charges. The dashed gray lines are the line degeneracies due to $G_i\mathcal{T}$, and the red spherical surfaces enclose the Z_2 monopoles.

tion and align the central singularities. The mapping of one quadrant is $\omega(k_x, k_y) \sim \text{Im}(\log[cn(z_i(k_x, k_y), \frac{1}{2})])$, where $z_1(k_x, k_y) = \frac{K(\frac{1}{2})}{\pi}(\frac{k_x - k_y}{2} + i\frac{k_x + k_y}{2})$ and K is the complete elliptic integrals of the first kind. The rest three quadrants are obtained by the translations of $z_2(k_x, k_y) = z_1(k_x + 2\pi, k_y)$, $z_3(k_x, k_y) = z_1(k_x, k_y + 2\pi)$, and $z_4(k_x, k_y) = z_1(k_x + 2\pi, k_y + 2\pi)$.

Experiments A photograph of the Dirac acoustic crystal is shown in Fig. 3(a), 3D-printed by the stereo lithography method using photocurable resin. The lattice constant is $a = 20\text{mm}$ and the fabrication error is $\pm 0.1\text{mm}$. The total size of the sample is $413.0\text{mm} \times 413.0\text{mm} \times 222.8\text{mm}$ containing $20 \times 20 \times 11$ cubic cells.

The surface states are measured through the Fourier-transformed field scan (FTFS). Similar approaches have been used to study other topological acoustic crystals [42–46]. A pressure-field microphone (diameter of 3.5mm, B&K-4138-A-015) is used as the scanning probe (receiver). The microphone is embedded in an aluminum alloy plate which works as a hard wall boundary on the top surface of the sample, as show in Fig. 3(a). The acoustic source is a broadband earphone, having frequency response up to 40kHz and a diameter of 5.5mm, fixed at the corner of the sample close to the plate. The

amplitude and phase of the pressure field are collected by the data acquisition module B&K-3160-A-042. A broadband signal is generated from the module and split into two channels, one to driven the earphone and the other as a time reference for the receiver. The frequency spectrum is averaged 100 times for each point scan and is normalized by the signal from the source.

The field scan is performed by moving the sample stage in three directions. During the collection of each data point, the sample is pressed towards the top plate to ensure the absence of air gaps. The scanning step is 5mm and the scanning range is 400mm in both x and y directions. Through 2D Fourier transforms, we obtain the spectral weight of the surface states in the momentum range of $(-2, 2)\frac{2\pi}{a}$. Similar to the processing technique used in Ref. [47], we patch the data of spatial scans to double the momentum resolution in the reciprocal space. In the x direction, we stitch two scanning fields of equivalent source positions. In the y direction, we rotate the data due to the C_2 symmetry on the surface.

The FTFS results are shown in three plots in Fig. 3 (d) (f) (h). The corresponding numerical results of the local density of states (LDOS)[48, 49] at the measurement interface are shown in Fig. 3 (c) (e) (g) respectively. The detailed algorithm of the surface LDOS will

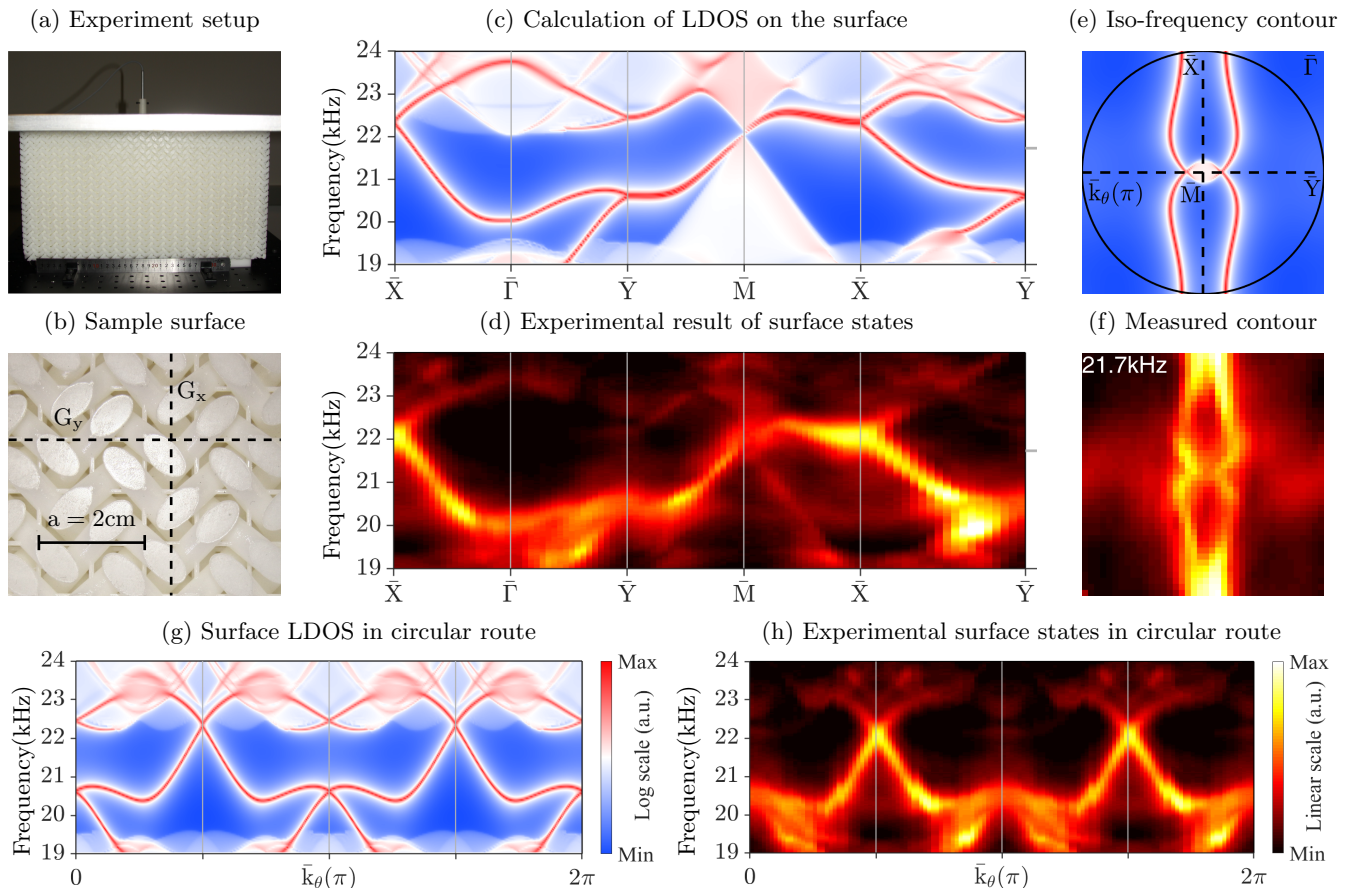


FIG. 3. Experiment observation of the quad-helicoid surface states by FTFS. (a) Photograph of the 3D-printed sample on the measurement setup. (b) Photograph of the sample surface. (c), (d) Numerical and experimental results of the surface states on the high-symmetry momentum lines. (e), (f) Numerical and experimental iso-frequency contour of the quad-helicoid surfaces showing four branches at 21.7kHz. (g), (h) Numerical and experimental results of the surface states in a circular route around the projected bulk Dirac points.

be presented in a separate paper. The agreement between experiments and numerics are visually obviously for the gapless surface dispersions.

Discussion We experimentally observed the first example of topological surface states associated with the 3D Dirac points. The line-degeneracy due to glide and \mathcal{T} symmetry is the key for stabilizing the gapless connection of helicoid sheets of opposite chiralities. Similarly, the other nonsymmorphic symmetry (screw rotation) and \mathcal{T} could also protect such line degeneracies when a domain wall is constructed to preserve the screw axis on the surface. It will also be interesting to explore the material realization of the double-helicoid surface states shown in Fig. 1(e), as well as helicoid surface states of Dirac semimetals [27].

This work establishes an ideal 3D Dirac material for consequent studies. For example, symmetry breakings of Dirac points can generate a variety of topological phenomena, such as the charged (Z or Z_2) nodal lines, nodal surfaces [50], Weyl dipoles as well as a gapped

bulk state supporting gapless surface [28] or chiral hinge modes [51, 52].

Acknowledgements We thank Timothy Hsieh and Liang Fu for the previous discussions on the $k \cdot p$ model. We are supported by the National key R&D Program of China under Grant No. 2017YFA0303800, 2016YFA0302400, 2016YFA0300600, by NSFC under Project No. 11974415, 11721404, 11674370, and by Chinese Academy of Sciences under grant number XXH13506-202.

* linglu@iphy.ac.cn

- [1] N. P. Armitage, E. J. Mele, and Ashvin Vishwanath. Weyl and dirac semimetals in three-dimensional solids. *Reviews of Modern Physics*, 90(1):15001, 2018.
- [2] ZK Liu, Bo Zhou, Yong Zhang, ZJ Wang, HM Weng, Dharmalingam Prabhakaran, S-K Mo, ZX Shen, Zhong Fang, Xi Dai, et al. Discovery of a three-dimensional topological dirac semimetal, na3bi. *Science*,

- 343(6173):864–867, 2014.
- [3] Madhab Neupane, Su Yang Xu, Raman Sankar, Nasser Alidoust, Guang Bian, Chang Liu, Ilya Belopolski, Tay Rong Chang, Horng Tay Jeng, Hsin Lin, Arun Bansil, Fangcheng Chou, and M. Zahid Hasan. Observation of a three-dimensional topological dirac semimetal phase in high-mobility cd3as2. *Nature Communications*, 5(1):3786, 2014.
 - [4] Zk Liu, J Jiang, B Zhou, Zj Wang, Y Zhang, Hm Weng, D Prabhakaran, Sk Mo, H Peng, P Dudin, T Kim, M Hoesch, Z Fang, X Dai, Zx Shen, Dl Feng, Z Hussain, and Yl Chen. A stable three-dimensional topological dirac semimetal cd3as2. *Nature Materials*, 13(7):677–681, 2014.
 - [5] Borisenko S, Gibson Q, Evtushinsky D, Zabolotnyy, Bchner B, and Cava Rj. Experimental realization of a three-dimensional dirac semimetal. *Physical Review Letters*, 113(2):27603, 2014.
 - [6] Su Yang Xu, Chang Liu, Satya K. Kushwaha, Raman Sankar, Jason W. Krizan, Ilya Belopolski, Madhab Neupane, Guang Bian, Nasser Alidoust, Tay Rong Chang, Horng Tay Jeng, Cheng Yi Huang, Wei Feng Tsai, Hsin Lin, Pavel P. Shibayev, Fang Cheng Chou, Robert J. Cava, and M. Zahid Hasan. Observation of fermi arc surface states in a topological metal. *Science*, 347(6219):294–298, 2015.
 - [7] Hemian Yi, Zhijun Wang, Chaoyu Chen, Youguo Shi, Ya Feng, Aiji Liang, Zhuojin Xie, Shaolong He, Junfeng He, Yingying Peng, Xu Liu, Yan Liu, Lin Zhao, Guodong Liu, Xiaoli Dong, Jun Zhang, M. Nakatake, M. Arita, K. Shimada, H. Namatame, M. Taniguchi, Zuyan Xu, Chuangtian Chen, Xi Dai, Zhong Fang, and X. J. Zhou. Evidence of topological surface state in three-dimensional dirac semimetal cd3as2. *Scientific Reports*, 4(1):6106–6106, 2015.
 - [8] Weiliang Yao, Chenyuan Li, Lichen Wang, Shangjie Xue, Yang Dan, Kazuki Iida, Kazuya Kamazawa, Kangkang Li, Chen Fang, and Yuan Li. Topological spin excitations in a three-dimensional antiferromagnet. *Nature Physics*, 14(10):1, 2018.
 - [9] Song Bao, Jinghui Wang, Wei Wang, Zhengwei Cai, Shichao Li, Zhen Ma, Di Wang, Kejing Ran, Zhao-Yang Dong, D. L. Abernathy, Shun-Li Yu, Xiangang Wan, Jian-Xin Li, and Jinsheng Wen. Discovery of coexisting dirac and triply degenerate magnons in a three-dimensional antiferromagnet. *Nature Communications*, 9(1):2591, 2018.
 - [10] Qinghua Guo, Oubo You, Biao Yang, James B. Sellman, Edward Blythe, Hongchao Liu, Yuanjiang Xiang, Jensen Li, Dianyuan Fan, Jing Chen, C. T. Chan, and Shuang Zhang. Observation of three-dimensional photonic dirac points and spin-polarized surface arcs. *Physical Review Letters*, 122(20), 2019.
 - [11] Steve M Young, Saad Zaheer, Jeffrey CY Teo, Charles L Kane, Eugene J Mele, and Andrew M Rappe. Dirac semimetal in three dimensions. *Physical review letters*, 108(14):140405, 2012.
 - [12] Zhijun Wang, Yan Sun, Xingqiu Chen, Cesare Franchini, Gang Xu, Hongming Weng, Xi Dai, and Zhong Fang. Dirac semimetal and topological phase transitions in a(3)bi (a = na, k, rb). *Physical Review B*, 85(19), 2012.
 - [13] Zhijun Wang, Hongming Weng, Quansheng Wu, Xi Dai, and Zhong Fang. Three-dimensional dirac semimetal and quantum transport in cd3as2. *Physical Review B*, 88(12), 2013.
 - [14] Julia A. Steinberg, Steve M. Young, Saad Zaheer, C. L. Kane, E. J. Mele, and Andrew M. Rappe. Bulk dirac points in distorted spinels. *Physical Review Letters*, 112(3):36403, 2014.
 - [15] HaiXiao Wang, Lin Xu, HuanYang Chen, and Jian-Hua Jiang. Three-dimensional photonic dirac points stabilized by point group symmetry. *Physical Review B*, 93(23):235155, 2016.
 - [16] Peizhe Tang, Quan Zhou, Gang Xu, and Shou-Cheng Zhang. Dirac fermions in an antiferromagnetic semimetal. *Nature Physics*, 12(12):1100–1104, 2016.
 - [17] Gang Li, Binghai Yan, Zhijun Wang, and Karsten Held. Topological dirac semimetal phase in pd and pt oxides. *Physical Review B*, 95(3):1–7, 2017.
 - [18] Alexey Slobozhanyuk, S. Hossein Mousavi, Xiang Ni, Daria Smirnova, Yuri S. Kivshar, and Alexander B. Khanikaev. Three-dimensional all-dielectric photonic topological insulator. *Nature Photonics*, 11(2):130–136, 2017.
 - [19] Qinghua Guo, Biao Yang, Lingbo Xia, Wenlong Gao, Hongchao Liu, Jing Chen, Yuanjiang Xiang, and Shuang Zhang. Three dimensional photonic dirac points in metamaterials. *Physical Review Letters*, 119(21), 2017.
 - [20] Hai-Xiao Wang, Yige Chen, Zhi Hong Hang, Hae-Young Kee, and Jian-Hua Jiang. Type-ii dirac photons. *npj Quantum Materials*, 2(1):54, 2017.
 - [21] Congcong Le, Xianxin Wu, Shengshan Qin, Yinxiang Li, Ronny Thomale, Fuchun Zhang, and Jiangping Hu. Dirac semimetal in -cui without surface fermi arcs. *Proceedings of the National Academy of Sciences of the United States of America*, 115(33):201803599, 2018.
 - [22] Peng Zhang, Zhijun Wang, Xianxin Wu, Koichiro Yaji, Yukiaki Ishida, Yoshimitsu Kohama, Guangyang Dai, Yue Sun, Cedric Bareille, Kenta Kuroda, Takeshi Kondo, Kozo Okazaki, Koichi Kindo, Xiancheng Wang, Changqing Jin, Jiangping Hu, Ronny Thomale, Kazuki Sumida, Shilong Wu, Koji Miyamoto, Taichi Okuda, Hong Ding, G.D. Gu, Tsuyoshi Tamegai, Takuto Kawakami, Masatoshi Sato, and Shik Shin. Multiple topological states in iron-based superconductors. *Nature Physics*, 15(1):41–47, 2019.
 - [23] Yihao Yang, Zhen Gao, Haoran Xue, Li Zhang, Mengjia He, Zhaoju Yang, Ranjan Singh, Yidong Chong, Baile Zhang, and Hongsheng Chen. Realization of a three-dimensional photonic topological insulator. *Nature*, 565(7741):622–626, 2019.
 - [24] Mehdi Kargarian, Mohit Randeria, and Yuan-Ming Lu. Are the surface fermi arcs in dirac semimetals topologically protected. *Proceedings of the National Academy of Sciences of the United States of America*, 113(31):8648–8652, 2016.
 - [25] Mehdi Kargarian, Yuan-Ming Lu, and Mohit Randeria. Deformation and stability of surface states in dirac semimetals. *Physical Review B*, 97(16):165129, 2018.
 - [26] Yun Wu, Na Hyun Jo, Lin-Lin Wang, Connor A. Schmidt, Kathryn M. Neilson, Benjamin Schruck, Przemyslaw Swatek, Andrew Eaton, S. L. Bud'ko, P. C. Canfield, and Adam Kaminski. Fragility of fermi arcs in dirac semimetals. *Physical Review B*, 99(16), 2019.
 - [27] Chen Fang, Ling Lu, Junwei Liu, and Liang Fu. Topological semimetals with helicoid surface states. *Nature Physics*, 12(10):936, 2016.

- [28] Ling Lu, Chen Fang, Liang Fu, Steven G Johnson, John D Joannopoulos, and Marin Soljačić. Symmetry-protected topological photonic crystal in three dimensions. *Nature Physics*, 12(4):337, 2016.
- [29] Ling Lu, Chen Fang, Timothy H. Hsieh, Liang Fu, Steven G. Johnson, John D. Joannopoulos, and Marin Soljai. Generalized three-dimensional dirac points and z_2 gapless surface states in a topological photonic crystal. In *2015 Conference on Lasers and Electro-Optics (CLEO)*, pages 1–2, 2015.
- [30] Boyuan Liu, J D Joannopoulos, Steven G Johnson, and Ling Lu. Generalized gilatraubenheimer method for density-of-states calculation in photonic crystals. *Journal of Optics*, 20(4):44005, 2018.
- [31] Takahiro Morimoto and Akira Furusaki. Weyl and dirac semimetals with z_2 topological charge. *Physical Review B*, 89(23), 2014.
- [32] Bohm-Jung Yang and Naoto Nagaosa. Classification of stable three-dimensional dirac semimetals with nontrivial topology. *Nature Communications*, 5(1):4898, 2014.
- [33] Bohm-Jung Yang, Takahiro Morimoto, and Akira Furusaki. Topological charges of three-dimensional dirac semimetals with rotation symmetry. *Physical Review B*, 92(16), 2015.
- [34] Rui Yu, Xiao Liang Qi, Andrei Bernevig, Zhong Fang, and Xi Dai. Equivalent expression of z_2 topological invariant for band insulators using the non-abelian berry connection. *Physical Review B*, 84(7):75119, 2011.
- [35] Chen Fang, Yige Chen, Hae-Young Kee, and Liang Fu. Topological nodal line semimetals with and without spin-orbital coupling. *Physical Review B*, 92(8):81201, 2015.
- [36] Kangkang Li, Chenyuan Li, Jiangping Hu, Yuan Li, and Chen Fang. Dirac and nodal line magnons in three-dimensional antiferromagnets. *Physical Review Letters*, 119(24), 2017.
- [37] Tom Bzduck and Manfred Sigrist. Robust doubly charged nodal lines and nodal surfaces in centrosymmetric systems. *Physical Review B*, 96(15):155105, 2017.
- [38] Zhida Song, Tiantian Zhang, and Chen Fang. Diagnosis for nonmagnetic topological semimetals in the absence of spin-orbital coupling. *Physical Review X*, 8(3), 2018.
- [39] Junyeong Ahn, Dongwook Kim, Youngkuk Kim, and Bohm-Jung Yang. Band topology and linking structure of nodal line semimetals with z_2 monopole charges. *Physical Review Letters*, 121(10), 2018.
- [40] Tiantian Zhang, Zhida Song, A Alexandradinata, Hongming Weng, Chen Fang, Ling Lu, and Zhong Fang. Double-weyl phonons in transition-metal monosilicides. *Physical review letters*, 120(1):016401, 2018.
- [41] Biao Yang, Qinghua Guo, Ben Tremain, Rongjuan Liu, Lauren E Barr, Qinghui Yan, Wenlong Gao, Hongchao Liu, Yuanjiang Xiang, Jing Chen, et al. Ideal weyl points and helicoid surface states in artificial photonic crystal structures. *Science*, 359(6379):1013–1016, 2018.
- [42] Feng Li, Xueqin Huang, Jiuyang Lu, Jiahong Ma, and Zhengyou Liu. Weyl points and fermi arcs in a chiral phononic crystal. *Nature Physics*, 14(1):30–34, 2018.
- [43] Hao Ge, Xu Ni, Yuan Tian, Samit Kumar Gupta, Ming-Hui Lu, Xin Lin, Wei-Dong Huang, C. T. Chan, and Yan-Feng Chen. Experimental observation of acoustic weyl points and topological surface states. *Physical review applied*, 10(1), 2018.
- [44] Yihao Yang, Hong xiang Sun, Jian ping Xia, Haoran Xue, Zhen Gao, Yong Ge, Ding Jia, Shou qi Yuan, Yidong Chong, and Baile Zhang. Topological triply degenerate point with double fermi arcs. *Nature Physics*, page 1, 2019.
- [45] Valerio Peri, Marc Serra-Garcia, Roni Ilan, and Sebastian D. Huber. Axial-field-induced chiral channels in an acoustic weyl system. *Nature Physics*, 15(4):357–361, 2019.
- [46] Boyang Xie, Hui Liu, Hua Cheng, Zhengyou Liu, Shuqi Chen, and Jianguo Tian. Experimental realization of type-II weyl points and fermi arcs in phononic crystal. *Physical Review Letters*, 122(10), 2019.
- [47] Qinghui Yan, Rongjuan Liu, Zhongbo Yan, Boyuan Liu, Hongsheng Chen, Zhong Wang, and Ling Lu. Experimental discovery of nodal chains. *Nature Physics*, 14(5):461–464, 2018.
- [48] M P Lopez Sancho, J M Lopez Sancho, J M L Sancho, and J Rubio. Highly convergent schemes for the calculation of bulk and surface green functions. *Journal of Physics F: Metal Physics*, 15(4):851–858, apr 1985.
- [49] QuanSheng Wu, ShengNan Zhang, Hai-Feng Song, Matthias Troyer, and Alexey A. Soluyanov. Wanniertools : An open-source software package for novel topological materials. *Computer Physics Communications*, 224:405 – 416, 2018.
- [50] Meng Xiao and Shanhui Fan. Topologically charged nodal surface. *Preprint at arXiv: 1709.02363*, 2017.
- [51] Changming Yue, Yuanfeng Xu, Zhida Song, Hongming Weng, Yuan-Ming Lu, Chen Fang, and Xi Dai. Symmetry-enforced chiral hinge states and surface quantum anomalous hall effect in the magnetic axion insulator $\text{Bi}_2\text{Xsmxse}_3$. *Nature Physics*, 15(6):577–581, 2019.
- [52] Heejae Kim, Ken Shiozaki, and Shuichi Murakami. Glide-symmetric magnetic topological crystalline insulators with inversion symmetry. *Phys. Rev. B*, 100:165202, Oct 2019.

Discovering topological surface states of Dirac points: Supplementary material

Hengbin Cheng,^{1,2} Yixin Sha,³ Rongjuan Liu,¹ Chen Fang,¹ and Ling Lu^{1,4}

¹*Institute of Physics, Chinese Academy of Sciences/Beijing National
Laboratory for Condensed Matter Physics, Beijing 100190, China*

²*School of Physical Sciences, University of Chinese Academy of Sciences, Beijing 100049, China*

³*School of Electronics Engineering and Computer Science, Peking University, Beijing 100871, China*

⁴*Songshan Lake Materials Laboratory, Dongguan, Guangdong 523808, China.*

I. UNIT CELL DESIGN

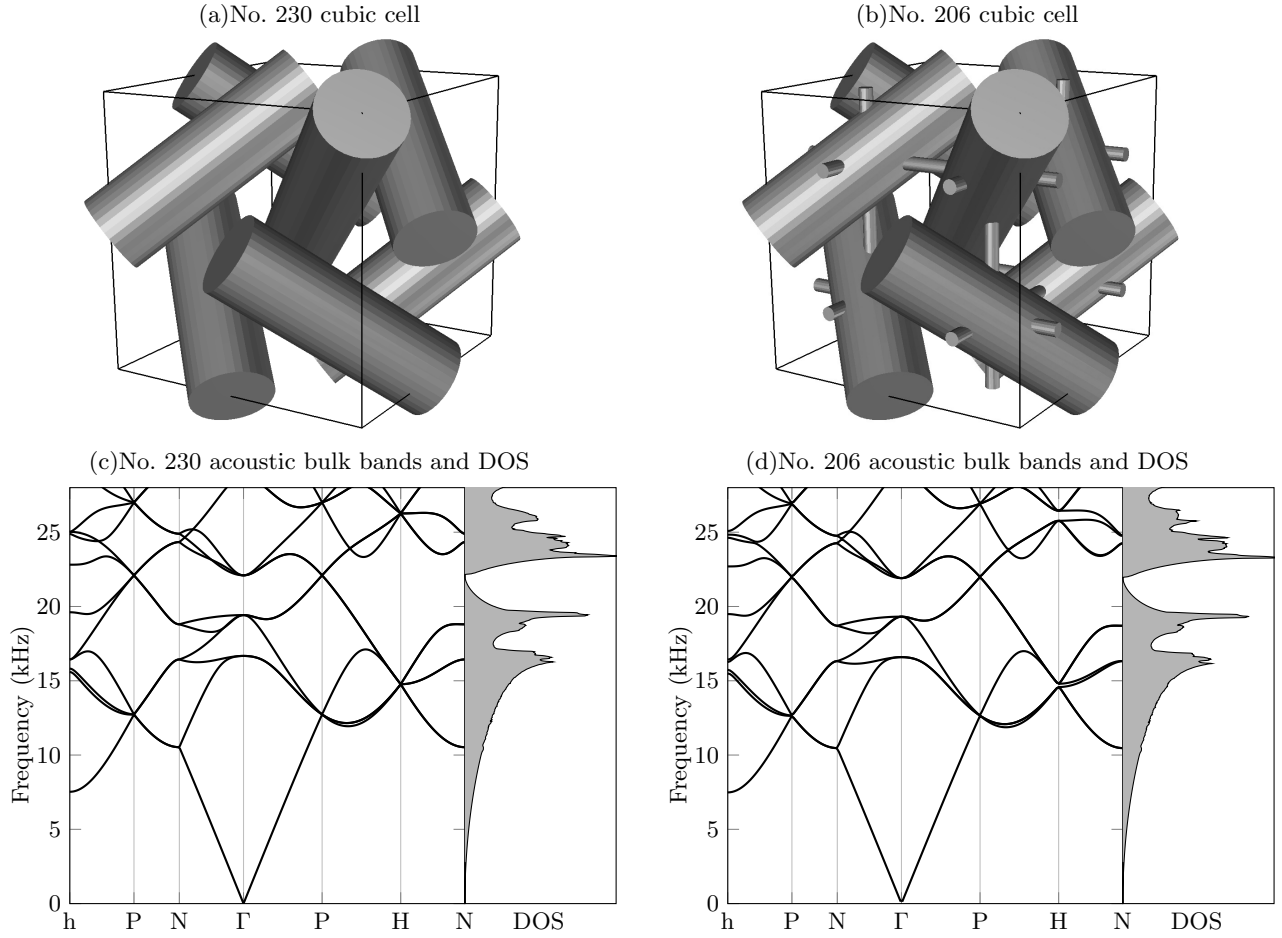


FIG. S1: Design of ideal acoustic Dirac point without and with the thin sticks. (a), (c) BPI acoustic crystal of space group No. 230. (b), (d) Thin-stick joined BPI acoustic crystal of space group No. 206.

For sample stability, we add the 12 thin sticks of radius $0.025a$ (1mm in experiment) to connect all the BPI rods. Fig. S1(a), (b) are the unit-cell structures without and with thin sticks, they belong to space group No. 230 and No. 206 respectively. The thin sticks preserve the three glides that protect the ideal Dirac points. The corresponding acoustic bulk bands are plotted in Fig. S1(c), (d), which are almost identical for the frequency range of the Dirac points.

II. $\mathbf{k} \cdot \mathbf{p}$ MODEL

The local dispersion and topology at P point can be described by the effective Hamiltonian of $\mathbf{k} \cdot \mathbf{p}$ model, written as $H(\mathbf{k}) = A\mathbf{k} \cdot \mathbf{p}$, considering the first non-zero order of \mathbf{k} . Here, we show the detailed derivation of the effective Hamiltonian of our ideal acoustic Dirac point in space group $Ia\bar{3}d$ (No. 230) and $Ia\bar{3}$ (No. 206).

Considering the space group $Ia\bar{3}d$ (No. 230), we choose four independent symmetry operations (generators) of the little group at momentum point P . They are two-fold rotation symmetry $C_{2z} = \{C_2|(0, \frac{1}{2}, 0)\}$ along [001] direction, two-fold rotation symmetry $C_{2y} = \{C_2|(\frac{1}{2}, 0, 0)\}$ along [010] direction, three-fold rotation symmetry C_3 along [111] direction and glide reflection symmetry $G = \{M|(-\frac{3}{4}, -\frac{3}{4}, \frac{1}{4})\}$ in $[1\bar{1}0]$ plane. Here G is different from the G_i ($i = x, y, z$) glides in [100], [010], [001] planes. P point has no G_i ($i = x, y, z$) symmetries, but has $G_i\mathcal{T}$ that can be obtained by $G_i\mathcal{T} = C_{2i} \cdot \mathcal{PT}$ ($i = x, y, z$). \mathcal{PT} is the parity-time symmetry preserves in the whole BZ.

P point has \mathcal{PT} but has neither \mathcal{P} nor \mathcal{T} . \mathcal{PT} is an anti-unitary operator which can be written as $\mathcal{PT} = U \cdot \mathcal{K}$, where U is a unitary matrix and \mathcal{K} is the complex conjugate. The little group of P point has two conjugated 2D representations, forming a 4D representation under \mathcal{PT} . We obtain the irreducible representation (Irrep) matrices of the selected generators from Bilbao crystal server, noted as Bilbao Rep. in Table II. After unitary transformations, we have the representation matrices in real basis (Real Rep.) and in Dirac basis (Dirac Rep.).

Operators	Bilbao Rep.	Real Rep.	Dirac Rep.
C_{2z}	$\begin{pmatrix} i & 0 & 0 & 0 \\ 0 & -i & 0 & 0 \\ \hline 0 & 0 & i & 0 \\ 0 & 0 & 0 & -i \end{pmatrix}$	$\begin{pmatrix} 0 & 0 & 0 & 1 \\ 0 & 0 & 1 & 0 \\ 0 & -1 & 0 & 0 \\ -1 & 0 & 0 & 0 \end{pmatrix}$	$\begin{pmatrix} i & 0 & 0 & 0 \\ 0 & -i & 0 & 0 \\ 0 & 0 & i & 0 \\ 0 & 0 & 0 & -i \end{pmatrix}$
C_{2y}	$\begin{pmatrix} 0 & i & 0 & 0 \\ i & 0 & 0 & 0 \\ \hline 0 & 0 & 0 & i \\ 0 & 0 & i & 0 \end{pmatrix}$	$\begin{pmatrix} 0 & 0 & -1 & 0 \\ 0 & 0 & 0 & 1 \\ 1 & 0 & 0 & 0 \\ 0 & -1 & 0 & 0 \end{pmatrix}$	$\begin{pmatrix} 0 & -1 & 0 & 0 \\ 1 & 0 & 0 & 0 \\ 0 & 0 & 0 & -1 \\ 0 & 0 & 1 & 0 \end{pmatrix}$
C_3	$\frac{1}{\sqrt{2}} \begin{pmatrix} e^{i\frac{3}{4}\pi} & e^{i\frac{7}{4}\pi} & 0 & 0 \\ e^{i\frac{5}{4}\pi} & e^{i\frac{5}{4}\pi} & 0 & 0 \\ \hline 0 & 0 & e^{i\frac{3}{4}\pi} & e^{i\frac{7}{4}\pi} \\ 0 & 0 & e^{i\frac{5}{4}\pi} & e^{i\frac{5}{4}\pi} \end{pmatrix}$	$\frac{1}{2} \begin{pmatrix} -1 & -1 & -1 & -1 \\ 1 & -1 & -1 & 1 \\ 1 & 1 & -1 & -1 \\ 1 & -1 & 1 & -1 \end{pmatrix}$	$\frac{-1}{2} \begin{pmatrix} 1-i & -1-i & 0 & 0 \\ 1-i & 1+i & 0 & 0 \\ 0 & 0 & 1-i & -1-i \\ 0 & 0 & 1-i & 1+i \end{pmatrix}$
G	$\begin{pmatrix} 0 & 1 & 0 & 0 \\ i & 0 & 0 & 0 \\ \hline 0 & 0 & 0 & -1 \\ 0 & 0 & -i & 0 \end{pmatrix}$	$\frac{-1}{2} \begin{pmatrix} 0 & 1+i & 0 & 1+i \\ 1+i & 0 & -1-i & 0 \\ 0 & -1-i & 0 & 1+i \\ 1+i & 0 & 1+i & 0 \end{pmatrix}$	$\begin{pmatrix} 0 & 0 & 0 & -i \\ 0 & 0 & -1 & 0 \\ 0 & -i & 0 & 0 \\ -1 & 0 & 0 & 0 \end{pmatrix}$
\mathcal{PT}	$\Gamma_{22}\mathcal{K}$	\mathcal{K} (complex conjugate)	$\Gamma_{22}\mathcal{K}$
$H(\mathbf{k})$	$(\sigma_x + w\sigma_y) \otimes (k_x\sigma_z + k_y\sigma_x - k_z\sigma_y)$	$(-k_x\Gamma_{10} - k_y\Gamma_{33} + k_z\Gamma_{31}) + w(-k_x\Gamma_{30} + k_y\Gamma_{13} - k_z\Gamma_{11})$	$\sqrt{1+w^2}\sigma_z \otimes \mathbf{k} \cdot \boldsymbol{\sigma}$
mass	$m\Gamma_{30} + m'(\Gamma_{20} - w\Gamma_{10})$	$m\Gamma_{20} + m'(\Gamma_{32} - w\Gamma_{12})$	$m\Gamma_{10} + m'\Gamma_{20}$

TABLE I: Representation matrices of selected generators of the little group at P in space group No. 230. The four matrices in the gray cells are obtained from Bilbao website and the rest are worked out by commutation relations.

We need to find the representation matrix for \mathcal{PT} which is not given by Bilbao. We expand the 4D unitary U matrix by the 16 Gamma matrices with complex coefficients and determine the coefficients by the commutation relations in Table II.

	$\mathcal{PT} = U \cdot \mathcal{K}$		C_{2z}	C_{2y}	G	C_3
\mathcal{PT}	$\mathcal{PT}^2 = 1$	$UU^\dagger = 1$	$[C_{2z}, \mathcal{PT}] = 0$	$[C_{2y}, \mathcal{PT}] = 0$	$G(\mathcal{PT}) = i(\mathcal{PT})G$	$[C_3, \mathcal{PT}] = 0$

TABLE II: Compatibility relations used to determine \mathcal{PT} .

The sixteen Gamma matrices are $\Gamma_{ij} = \sigma_i \otimes \sigma_j$, ($i, j = 0, 1, 2, 3$), where $\sigma_0 = \begin{pmatrix} 1 & 0 \\ 0 & 1 \end{pmatrix}$, $\sigma_1 = \begin{pmatrix} 0 & 1 \\ 1 & 0 \end{pmatrix}$, $\sigma_2 = \begin{pmatrix} 0 & -i \\ i & 0 \end{pmatrix}$, $\sigma_3 = \begin{pmatrix} 1 & 0 \\ 0 & -1 \end{pmatrix}$, and \otimes is the Kronecker product.

The Hamiltonian can be written as $H(\mathbf{k}) = A(k_x p_x + k_y p_y + k_z p_z)$, where k_x, k_y, k_z are three real variables (the origin is set at P in below), and p_x, p_y, p_z are three Hermitian matrices. To find p_x, p_y, p_z , we expand them as

linear combinations of 16 Gamma matrices with real coefficients and determine the coefficient by the commutation relations in Table. III.

For any representation matrix $D(g)$ of symmetry operation g (including \mathcal{PT}) in the little group, we have

$$D(g)H(\mathbf{k})D^{-1}(g) = H(g\mathbf{k}) \quad (1)$$

that gives the following commutation ($[\]=0$) and anti-commutation ($\{\ }=0$) relations, listed in Table. III.

	p_z	p_y	p_x
\mathcal{PT}	$[\mathcal{PT}, p_z] = 0$	$[\mathcal{PT}, p_y] = 0$	$[\mathcal{PT}, p_x] = 0$
C_{2z}	$[C_{2z}, p_z] = 0$	$\{C_{2z}, p_y\} = 0$	$\{C_{2z}, p_x\} = 0$
C_{2y}	$\{C_{2y}, p_z\} = 0$	$[C_{2y}, p_y] = 0$	$\{C_{2y}, p_x\} = 0$
G	$[G, p_z] = 0$	$Gp_y = p_xG$	
C_3	$p_y = C_3^{-1}p_zC_3, p_x = C_3p_zC_3^{-1}$		

TABLE III: Compatibility relations used to determine $H(\mathbf{k})$.

By satisfying all the requirements in Table. III, for Bilbao Rep. we obtain $p_z = \Gamma_{13} + w\Gamma_{23}$, ($w \in \mathbb{R}$). p_x and p_y are obtained from p_z by C_3 symmetry. Ignore the constant term A , the effective Hamiltonian is given as

$$H_D(\mathbf{k}) \sim (\sigma_x + w\sigma_y) \otimes (k_z\sigma_z + k_x\sigma_y - k_y\sigma_x) \quad (2)$$

After an unitary transformation, we get the representation matrix under Dirac Rep.

$$H_D(\mathbf{k}) \sim \sqrt{1+w^2} \begin{pmatrix} \mathbf{k} \cdot \boldsymbol{\sigma} & 0 \\ 0 & -\mathbf{k} \cdot \boldsymbol{\sigma} \end{pmatrix} \quad (3)$$

where $w \in \mathbb{R}$ is the velocity term. Note that the Dirac Hamiltonian we obtained above satisfies the exact massless Dirac equation in 3D. What listed in the last row of Table. I are the matrix of the Dirac mass terms, in corresponding basis with coefficients $m, m' \in \mathbb{R}$.

For space group No. 206, the only missing generators is $G = \{M|(-\frac{3}{4}, -\frac{3}{4}, \frac{1}{4})\}$ in $[1\bar{1}0]$ plane, and the Dirac Hamiltonian under Bilbao Rep. is

$$H_D(\mathbf{k}) \sim (\sigma_x + w\sigma_y + u\sigma_z) \otimes (k_z\sigma_z - k_x\sigma_x - k_y\sigma_y), \quad (w, u \in \mathbb{R}) \quad (4)$$

. After an unitary transformation, we have the representation matrix under Dirac Rep.

$$H_D(\mathbf{k}) \sim \sqrt{1+w^2+u^2} \begin{pmatrix} \mathbf{k} \cdot \boldsymbol{\sigma} & 0 \\ 0 & -\mathbf{k} \cdot \boldsymbol{\sigma} \end{pmatrix} \quad (5)$$

III. DIRAC POINT UNDER SYMMETRY BREAKINGS

Dirac point lies in the phase transition center of many topological band nodal structures. In Table. IV we list the possible four bands nodal structures that can be achieved from perturbing the Dirac point, and list the corresponding key symmetries that need to be preserved(\checkmark) or broken(\times).

	Z_2 Dirac point	Z_2 nodal ring	Z_2 Weyl dipole	gapped Dirac	gapped	Weyl points	nodal ring
Z_2	1			0			
Realization	Fig. 2(a)	Fig. 2(b)	Fig. 2(c)	Fig. 2(d)	-	-	-
Space group	No. 230	No. 088	No. 120	No. 220	-	-	-
	No. 206	No. 015	No. 045	No. 199	-	-	-
\mathcal{PT}	\checkmark	\checkmark	\times	\times	\times	\times	\checkmark
$G_i\mathcal{T}$	\checkmark	\checkmark	\times	\times	\times	\times	\times
$G_{j,k}\mathcal{T}$	\checkmark	\times	\checkmark	\times	\times	\times	\times
C_3	\checkmark	\times	\times	\checkmark	\times	\times	\times
l_0, l_1, l_2	0, 0, 0	$l_0, 0, 0$	$0, l_1, 0$	$0, 0, l_2$	$0, l_1 < l_2 $	$0, l_1 > l_2 $	-
Hamiltonian	$H(\mathbf{k}) \sim H_D(\mathbf{k}) + l_0\Gamma_{13} + l_1\Gamma_{03} + l_2\Gamma_{30}, \quad (l_0, l_1, l_2 \in \mathfrak{R})$ $H_D(\mathbf{k}) \sim (\sigma_x + w\sigma_y) \otimes (k_z\sigma_z + k_x\sigma_y - k_y\sigma_x)$						

TABLE IV: Possible results of the Dirac point transition under symmetry breaking.

IV. REALIZATION OF VARIOUS SYMMETRY BREAKINGS

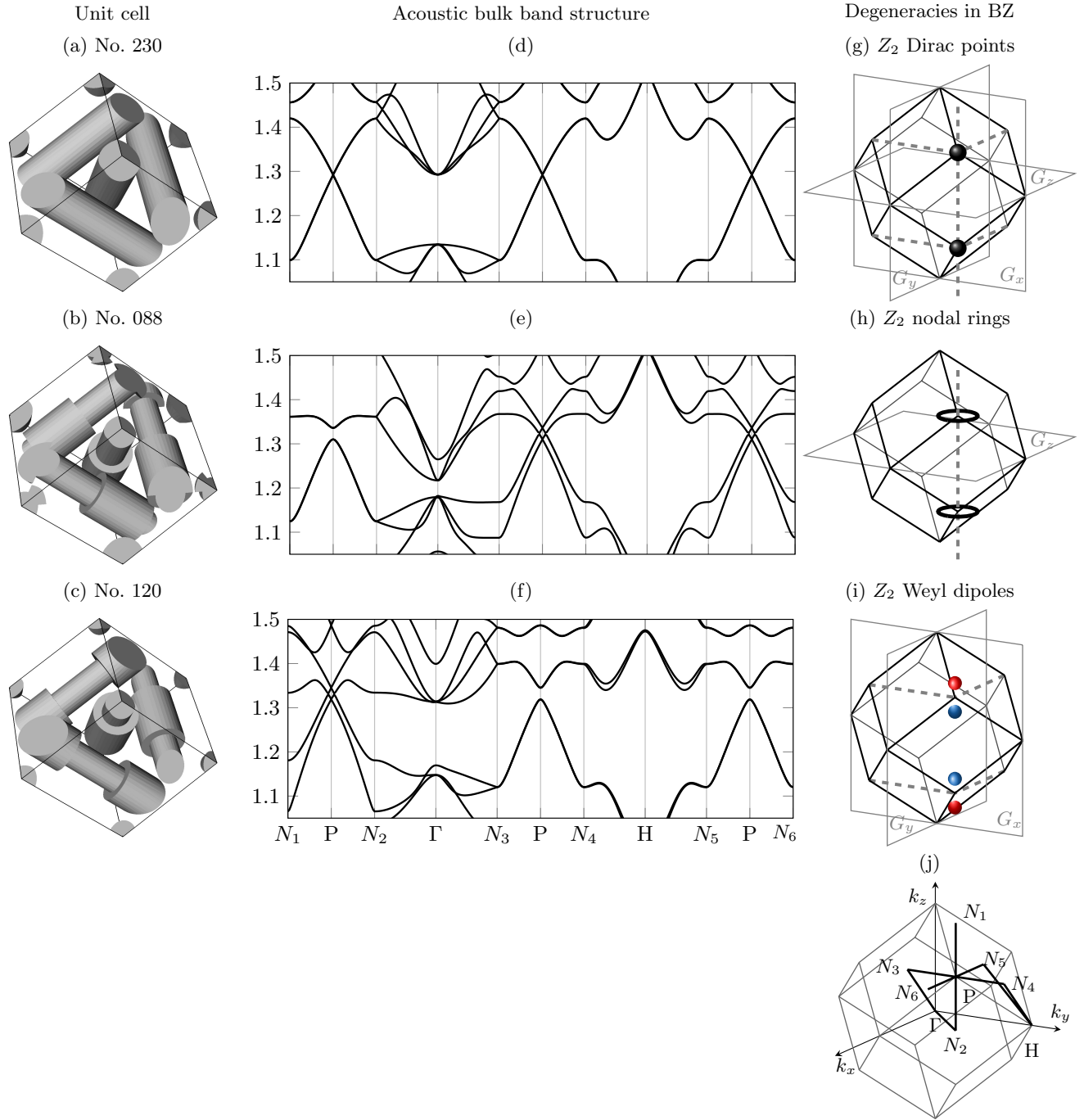


FIG. S2: Realization of the predicted symmetry breaking results. (a), (d), (g) Two Dirac points (black spheres) in the first BZ, locate at point $\pm P$. The dashed gray lines denote for the $G_i\mathcal{T}$ stabilized line degeneracies. (b), (e), (h) The Dirac points turn into Z_2 nodal rings (black circle). The $G_z\mathcal{T}$ stabilized degenerate lines, between lower or higher two bands, perpendicularly cross the rings and form nodal links within the four bands. (c),(f),(i) The Dirac points split into Z_2 Weyl dipoles (blue and red spheres for opposite chiralities). Since the two surface glides are not broken, the quad-helicoid surface states are still robust. Note that each one of $G_x\mathcal{T}$, $G_y\mathcal{T}$ is enough for keeping the Z_2 Weyl dipoles, but we need both to keep the quad-helicoid on 001 surface.

V. COMPARISON OF EIGENVALUE AND LDOS CALCULATIONS

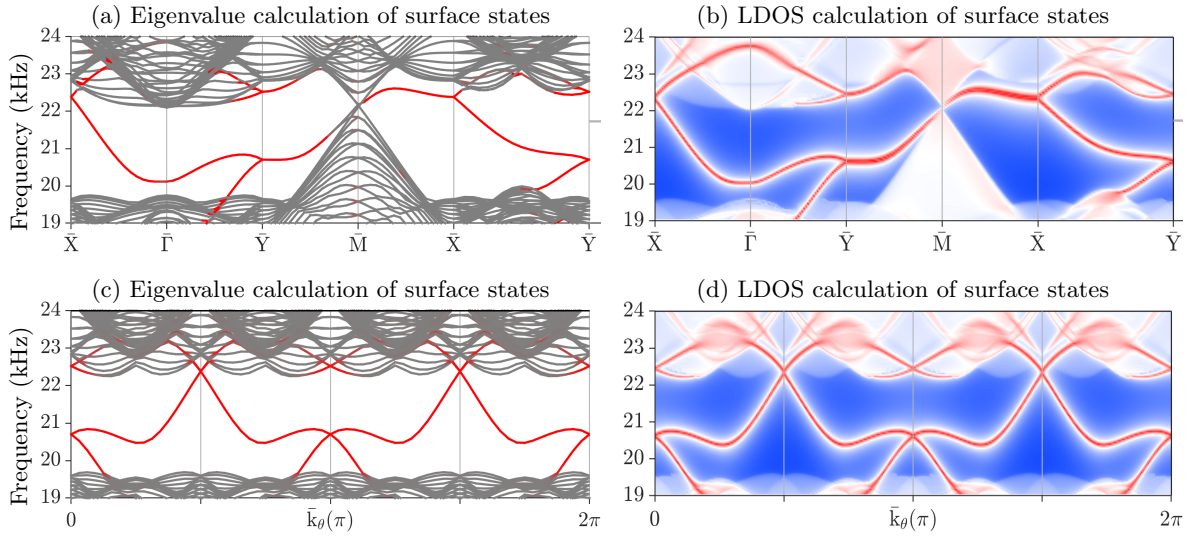


FIG. S3: Surface states in eigenvalue solutions and LDOS results. (a),(c) The surface states dispersion are obtained by solving the eigenvalue equation for a ten cubic cell stack with Floquet periodic boundary conditions in x and y directions and hard-wall boundaries on z and -z ends. The dispersion lines were colored in red if they have a large energy fraction in the first two cells on the surface. The results agree the local density of states (LDOS) results in (b),(d), respectively.

VI. ADDITIONAL EXPERIMENTAL RESULTS

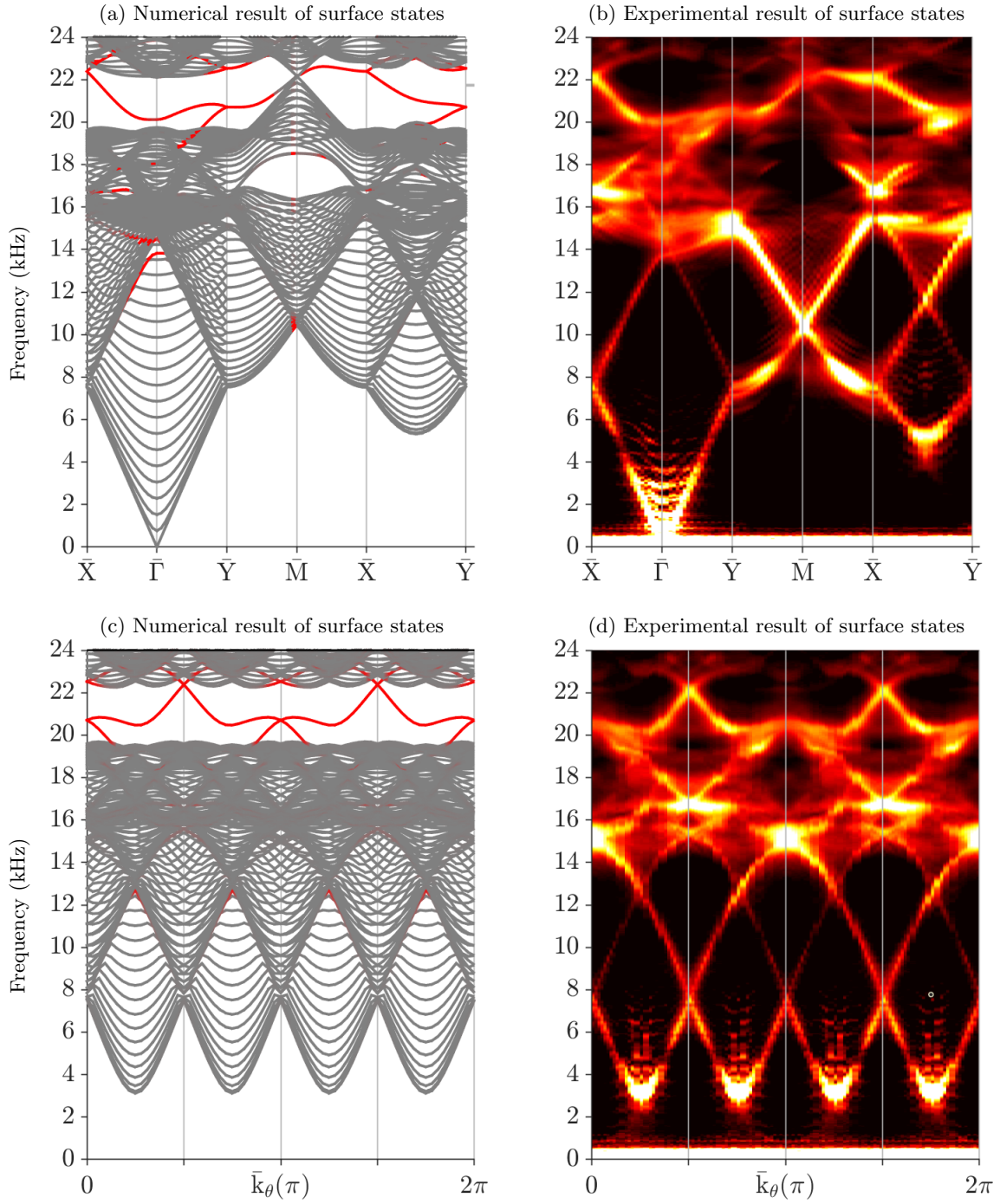


FIG. S4: Full frequency range data of the numerical and measured surface states.

VII. MORE DETAILS ON EXPERIMENTAL MEASUREMENTS

	Mass density ρ (kg/m^3)	Longitudinal sound velocity v_L (m/s)	Acoustic impedance $Z = \rho \cdot v_L$ ($N \cdot s/m^3$)
Air	1.2	343	412
Cured resin	~ 1140	~ 2240	$\sim 2.55e6$

TABLE V: Material properties of air and cured resin of 3D printing. Due to the 6200 times higher acoustic impedance of resin, the air-resin interface can be treated as hard-wall boundary conditions in calculations. The pressure field inside the resin are ignored.

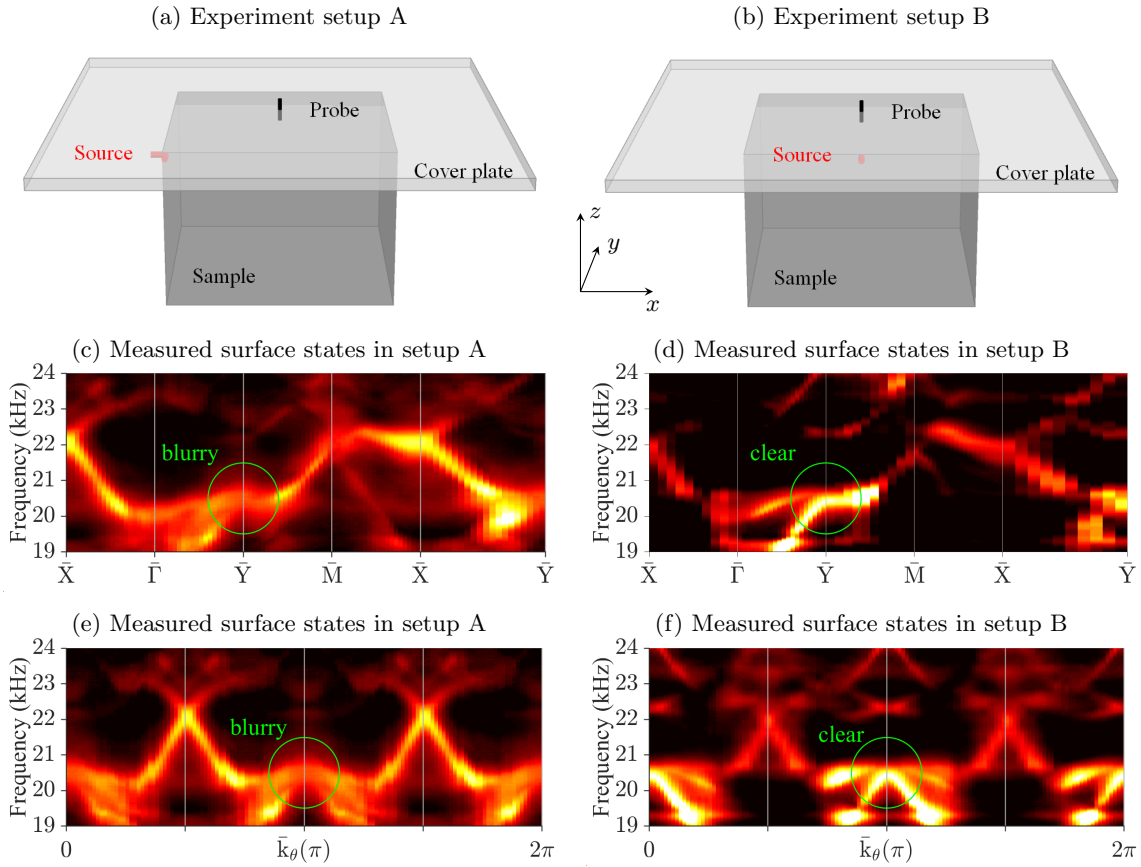


FIG. S5: Experimental data from different positions of the source excitations. (a) Setup A with the source fixed at the top corner of the sample, whose measurement results are shown in (c) and (e). (b) Setup B with the source fixed at the center of top edge of the sample, whose measurement results are shown in (d) and (f).